Active control of flow over a backward-facing step at high Reynolds numbers

Thomas McQueen [a],[*], David Burton [b], John Sheridan [a], Mark C. Thompson [a]

[a] *Fluids Laboratory for Aeronautical and Industrial Research (FLAIR), Department of Mechanical and Aerospace Engineering, Monash University, Clayton 3800, Australia*
[b] *Monash Wind Tunnel Research Platform (MWTRP), Department of Mechanical and Aerospace Engineering, Monash University, Clayton 3800, Australia*

ARTICLE INFO

ABSTRACT

This work provides new insight into the transient flow effects of forcing a backward-facing step flow at high Reynolds number. The detailed flow structure and surface pressure is investigated over the range $118,000 \leqslant Re_H \leqslant 472,000$ using time-resolved particle-image velocimetry. Notably, this research considerably extends the Reynolds number ranges of previous studies. The effect of periodic shear-layer forcing on the global mean and fluctuating flow structure is examined over the forcing frequency range $0.036 \leqslant St_H \leqslant 1.98$. The effect of forcing on the base pressure, which has received relatively little attention, is also detailed. These studies allow us to characterise the relationship between the forcing frequencies, with a particular focus on frequencies near and significantly above the shear-layer instability. Importantly, despite the high Reynolds number, we are able to perturb the shear layer to control both the reattachment length and base pressure. Forcing at frequencies close to the shear-layer instability results in a significant reattachment length reduction, as has been well reported, with a corresponding base pressure reduction of up to 45%. At the highest forcing frequency, an increase in mean base pressure of 9.7% is found, with a corresponding increase in reattachment length of 3.9% over the unforced case. This high-frequency forcing reduced initial growth of the shear-layer instability and stabilised the latter half of the reattachment zone. This enabled more flow entrainment upstream to the step-base, resulting in a mean base-pressure increase. Although, this came at the cost of triple the base-pressure fluctuations, an important insight for practical flow-control applications. The spatial distribution of spectral power for key instabilities in the flow, and the influence of forcing on these distributions, is also examined. To our knowledge, the spatial distribution of these key instabilities, with or without control, has not been previously presented for high Reynolds numbers ($Re_H > 10^4$).

1. Introduction

The backward-facing step (BFS) is one of the most prevalent geometries studied in fluid mechanics. This interest arises primarily because the geometry displays key flow features of more complex geometries/separated flows. These include a fixed separation point, recirculation zone, reattachment zone, and a redeveloping boundary layer. Both the time-averaged and dynamic aspects of these flow features, along with the various geometric and flow parameters that affect the flow structure, have been extensively studied.

While the geometry of a BFS is inherently simple, various factors can alter the resultant flow structure significantly. In particular: the ratio of step height to width, termed the aspect ratio (*AR*); the pressure gradient,

primarily a function of the ratio between channel height upstream and downstream of the step, termed the expansion ratio (*ER*); the initial boundary-layer state; the boundary-layer thickness (δ); and free-stream turbulence levels, have been identified as key parameters affecting the separated flow (Eaton and Johnston, 1981). In addition, the global flow structure has been shown to vary with Reynolds number (*Re*) (Chovet et al., 2017; Nadge and Govardhan, 2014). Predominately, the geometry has been employed to conduct fundamental studies on separated flow, where one or more of the aforementioned parameters are systematically varied. In other instances, one or more of the parameters have been tailored to provide a simplified representation of more complex geometries such as buildings, vehicles, and combustion chambers.

At very small Reynolds numbers, the flow over a BFS is initially

---

steady, although instabilities quickly evolve (Barkley et al., 2002). A turbulent regime soon ensues, and by the higher Reynolds numbers of interest in this study, the separated shear layer is fully turbulent. Chandrsuda and Bradshaw (1981) demonstrated that the separated flow initially resembles that of a plane mixing layer, with significant differences only becoming apparent in the region near reattachment, where the separated shear layer bends downward and impinges upon the wall. In the reattachment zone, flow is both drawn back upstream, due to a high adverse pressure gradient, and convected downstream (Nash, 1963). Upstream of reattachment, a well-defined recirculation bubble, with a smaller secondary bubble in the bottom corner of the step, exists in the mean sense (Nadge and Govardhan, 2014).

Along the step floor, the minimum pressure is located in the recirculation region at approximately half the reattachment length (X_r). Thereafter, the pressure rises to a maximum past reattachment. Nash (1963) discussed how the concave curvature of the external streamlines and resulting increase in the stream-tube area near the reattachment point give rise to an overshoot in the pressure distribution along the wall. It was also noted that the rise in pressure over the reattachment region enables the transport of fluid back upstream into the recirculation zone.

In addition to the time-averaged flow features, the dynamics of the BFS flow have also been extensively studied. Hasan (1992) discussed how the reattaching shear layer behind the BFS has two distinct modes of instability. The first mode is a Kelvin–Helmholtz instability, evident in the free-shear layer formed at separation. This instability was found to scale with momentum thickness at separation at a reduced frequency of $St_\theta \approx 0.012$. The second instability is apparent further downstream and was found to scale with the step height at a reduced frequency of $St_H \approx 0.185$. Hasan (1992) proposed that this second instability formed due to a vortex merging process in the shear layer. A pairing of vortices initially occurs in the shear layer. However, as the shear layer approaches the wall, further pairing is inhibited (Troutt et al., 1984). Furthermore, a broadband low-frequency 'flapping' motion of the recirculation zone has been identified by several authors. Ma and Schröder (2017) collated various hypotheses that have been proposed to explain the flapping phenomenon and conducted their own experiments to provide further insight. They found that the shear layer begins to flap up and down starting from the middle of the recirculation region, where its spatial development reaches a scale equivalent to the step height. The flapping motion alters the recirculation structure, changing the instantaneous reattachment point. The flapping motion was attributed to an absolute instability, first identified by Wee et al. (2004), with a peak growth rate in the proximity of the maximum reverse flow in the recirculation zone.

There have been many studies at Reynolds numbers (based on step height) up to approximately $Re_H = 10^4$, but only a few detailing the response of the flow at higher values. Nadge and Govardhan (2014) examined the flow over $5.0 \times 10^3 \leqslant Re_H \leqslant 6.7 \times 10^4$. They suggested that the reattachment length saturates for values above $Re_H > 2 \times 10^4$, and that once the boundary layer is turbulent, no appreciable variation in the flow structure occurs with further increasing Reynolds number. More recently, Chovet et al. (2017) conducted a similar investigation over the range $3.15 \times 10^4 \leqslant Re_H \leqslant 1.83 \times 10^5$. For $Re_H > 10^5$, they found that the reattachment length had not stabilised, but rather there was a gradual decrease up to the highest Reynolds number investigated. Variation in the flow dynamics was also observed, with a relative increase in energy associated with the flapping motion in comparison to higher frequency shedding for higher Reynolds numbers. It remains unknown whether the trend in decreasing reattachment length continues for higher Reynolds numbers.

Due to its geometric simplicity and the previously mentioned presence of some key features of separated flows in general, the BFS has also been used to examine the effectiveness of both passive and active flow-control techniques. Using periodic forcing, researchers have been able to

alter the characteristics of the recirculation zone and the reattachment length [e.g.,] (Chun and Sung, 1996; Yoshioka et al., 2001; Chovet et al., 2017). By amplifying the primary shear-layer instability and increasing momentum entrainment into the recirculation zone, reductions in reattachment length in the order of 50% have been achieved. Using higher frequency forcing, researchers have also been able to achieve a smaller increase in reattachment length. Berk et al. (2017) attributed this increase to a decrease in entrainment into the recirculation zone and attenuation of incoming perturbations due to the high-frequency forcing.

The majority of past work on forced flow over a BFS has focused on changes in reattachment length and global flow structure, which has revealed key insights into the behaviour of separated flows. However, the effect of forcing on the base pressure has perhaps received less attention than merited, given its importance in practical applications such as bluff-body drag reduction or structural loading. One study with a focus on base pressure was the work conducted by Dahan et al. (2012), who were able to increase the base pressure of the BFS by up to 20% using both open- and closed-loop control in three-dimensional simulations. Due to more direct application to road vehicle design, there has been significantly more focus on using flow-control techniques to increase the base pressure, and consequently reduce drag, of two- and three-dimensional bluff bodies. For a two-dimensional D-shaped body — with periodic forcing emanating from both the top and bottom edges of the base of the body — Pastoor et al. (2008) were able to increase the mean base pressure by 40% by delaying the formation of the alternating vortex street in the wake. For a three-dimensional body with imposed high-frequency forcing at the base of the body, Barros et al. (2016b) were able to reduce drag by 10% as a result of reduced shear-layer entrainment and a fluidic boat tailing effect. Comparable effects of high-frequency forcing for the BFS have been observed [i.e.,] (Berk et al., 2017), although the strategy of Pastoor et al. (2008) to delay the formation of the alternating vortex street is obviously not applicable to the wall-bounded recirculation zone of the BFS.

In this study, the flow over a BFS is investigated for Reynolds numbers over the range $1.18 \times 10^5 < Re_H < 4.72 \times 10^5$, higher than tested by recent studies employing imaging based analysis techniques such as particle image velocimetry (PIV). Surface flow visualisation, wall pressure measurements, and time-resolved PIV measurements are used to analyse the flow. This allows the spatial distribution of the spectral power of key dynamic flow features to be realised. Periodic active flow-control is introduced at the top corner of the step. In addition to examining the effects of Reynolds number and forcing on reattachment length and the global flow structure, the primary focus of this investigation is on determining the effect of forcing on the base pressure, targeting the development of fundamental flow-control strategies aimed at reducing drag or structural loading for geometries with separated flows. Lastly, the variation in instantaneous reattachment position and its relation to the base pressure dynamics are discussed. In this paper, the response with no imposed flow control is termed the 'natural' response.

2. Experimental set-up

The investigation was conducted in the *Monash Wind-Tunnel Research Platform* 2×2 wind tunnel. The wind tunnel is a closed circuit design with a 2 m × 2 m test section, 12 m in length. The model was installed on the floor of the wind tunnel with the vertical step face (base) located approximately 6 m downstream of the test section entrance. The model spanned the width of the test section. The height of the step, H, was 180 mm. A false floor extended 15 H upstream of the base. A ramp with a cubic spline profile connected the false floor to the wind tunnel floor. To reduce the size of the side wall boundary layers, splitter plates were installed 100 mm from each side wall. The splitters were 12 mm thick with a 4:1 elliptical leading edge. They extended 2 H upstream and 15 H downstream of the step base and to a height of 6 H above the step

floor. One splitter was made from acrylic to allow optical access for PIV measurements. The *AR* was 10, a value for which the flow is expected to be predominately two-dimensional over the mid section of the step span (De Brederode, 1975). This quasi two-dimensional behaviour of the flow over the mid-section was verified, in the mean sense, using a paint-drop surface flow visualisation technique. No appreciable mean spanwise component of surface shear-stress was identified for $\pm 1.5\,H$ from the model centre-line. Key parameters of the set-up are listed in Table 1, along with those for comparable studies referenced herein. Fig. 1 shows a schematic of the experimental set-up.

The reference velocity (U_{ref}), measured using a pitot tube located at $x/H = -3$, $y/H = 3$, and $z/H = -2.5$ was varied from 10 ms^{-1} to 40 ms^{-1}, resulting in a Reynolds number range based on the step height of $1.18 \times 10^5 < Re_H = \rho U_{\mathrm{ref}} H/\mu < 4.72 \times 10^5$ and a range based on momentum thickness at separation of $5.93 \times 10^3 < Re_\theta = \rho U_{\mathrm{ref}} \theta/\mu < 2.36 \times 10^4$, where θ is the momentum thickness. The incoming boundary layer was turbulent for all test configurations. For $Re_H = 2.4 \times 10^5$, the Reynolds number at which forcing was implemented and PIV measurements were obtained, the boundary-layer thickness was $\delta/H \approx 1.1$, and the momentum thickness was $\theta/H = 0.051$. The mean streamwise velocity and streamwise and wall-normal (y-direction) turbulence intensity profiles for the natural response (in the centre-line of the tunnel from $y/H = 0$ to wind-tunnel roof, one step height upstream of the base) were measured using a 4-hole dynamic pressure probe (Turbulent Flow Instrumentation, Cobra Probe) and are shown in Fig. 2. An overshoot in the velocity profile near the step can be observed. This overshoot is due to the presence of the ramp upstream of the step, and associated single-sided contraction of the wind tunnel. The streamwise and wall-normal components of turbulence intensity remained less than 0.8% and 1.3% respectively across the velocity range tested.

2.1. Actuation

The control flow was actuated by the emission of a pulsed jet from a 2 mm (0.011 H) wide slot (s) located at the top corner of the step (shown in Fig. 1). The slot exit was at an angle of 45° to the free-stream and extended continuously along the full 1800 mm width of the step. The pulsed jet was generated by eight speakers (Daichi, CS80) mounted below the step. Each speaker was individually tuned to ensure as even as possible velocity distribution across the length of the slot. Over the frequency range tested, there was no significant resonance that affected the distribution of the jet velocity. To ensure accurate slot dimensions and minimise deflection of the model during testing, the section of the model housing the speakers and slot was CNC machined from 12 mm thick steel plate. A waveform generator (Rigol, DS-1000Z) and power amplifier (Dayton Audio, MA1260) were used to generate a sinusoidal
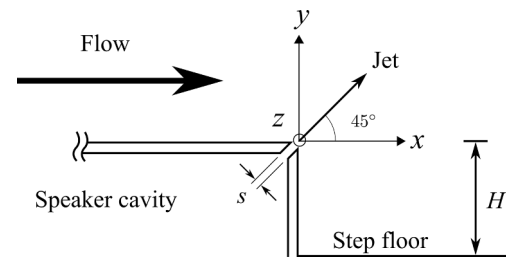

Fig. 1. Schematic of the experimental set-up detailing the coordinate system and key parameters. Not to scale.
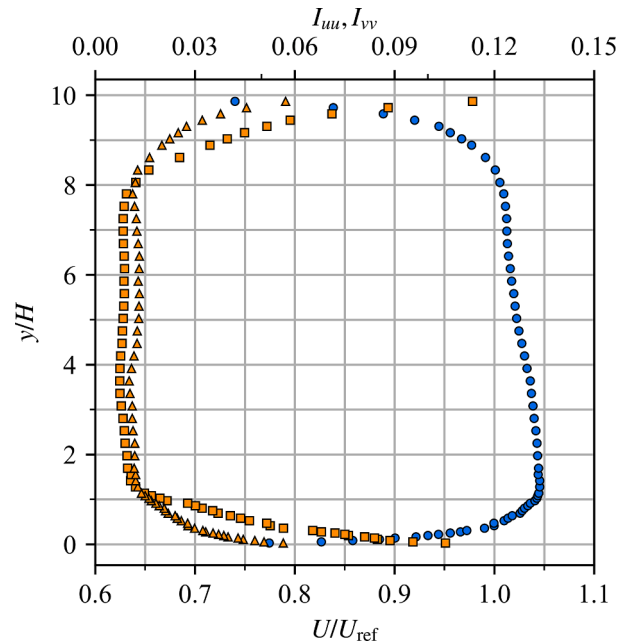

Fig. 2. Streamwise velocity profile (●), and streamwise (■) and wall-normal (▲) components of turbulence intensity at $x/H = -1$, from $y/H = 0$ to the w.ind-tunnel roof.

voltage profile which powered the speakers. Hot-wire thermal anemometry was used to characterise the relationship between speaker input voltage and peak jet velocity (U_j). The hot-wire probe was also used for point measurements in the flow field. The jet flow was characterised with zero free-stream velocity. A single wire probe (TSI, 1210-T1.5), mounted to a two-dimensional traverse system (with the wire positioned 2 mm from the slot exit), enabled the jet to be characterised in both the cross-jet and span-wise (z) directions. The peak jet velocity, defined as the peak velocity on the slot centre-line during the blowing phase, varied at most by $\pm 10\%$ from the span-wise average across the 10 H slot span. This variation was primarily due to differences in the response of the eight speakers. The forcing frequencies (f_j) are presented in non-dimensional form $St_H = f_j U_{\mathrm{ref}}/H$. Forcing frequencies from 4 Hz to 220 Hz ($0.036 \leqslant St_H \leqslant 1.98$) were implemented. The response of the flow to three forcing configurations in particular was examined in detail. The characteristics of these three frequencies are listed in Table 2. The

Table 1
Key parameters of the current and relevant studies.

Reference	ER	AR	δ/H	Re_H	Re_θ
Current study	1.10	10	1–1.1	1.18×10^5–4.72×10^5	5.93×10^3–2.36×10^4
Chovet et al. (2017)	1.04	24	0.47–0.68	3.15×10^4–1.83×10^5	—
Heenan and Morrison (1998)	1.1	12.2	0.21	1.9×10^5	4.06×10^3
Baker (1977)	1.07	18	0.7	5.00×10^4	—
Driver et al. (1987)	1.125	12	1.5	3.7×10^4	5.0×10^3
Nadge and Govardhan (2014)	1.10	60	0.65–0.76	6.70×10^3–3.40×10^4	7.80×10^2–2.58×10^3

Table 2
Key parameters of the three main forcing frequencies implemented.

Hz	St_H	U_j/U_{ref}	L_0/s
30	0.27	0.75	976 ± 98
100	0.90	0.75	269 ± 27
220	18	0.75	94 ± 9

pulsed jet is characterised by the non-dimensional stroke length, $L_0/s = \int_0^\tau u_0^2(t)dt$, where L_0 is the stroke length; $\tau = T/2$ is the time of half an actuation cycle (T), i.e., time of the blowing phase; and u_0 is the jet velocity, in this instance measured in the centre-line of the slot 2 mm from the slot exit (Smith and Glezer, 1998). Velocity profiles at the centre-line of the slot for the three main forcing configurations are shown in Fig. 3.

2.2. Flow measurements

Surface pressure was measured using a synchronous 128 channel Differential Pressure Measurement System (Turbulent Flow Instrumentation, DPMS) with each channel sampled at 3000 Hz for 120 seconds. Frequencies of up to 250 Hz were able to be resolved by applying amplitude and phase distortion corrections to account for tubing length. Pressure taps were located on the step base in $0.033H$ increments at $z/H = 0$ along $-1 < y/H < 0$, and on the step floor in $0.167H$ increments at $z/H = 0$ along $0 < x/H < 10$.

The streamwise and wall-normal components of the velocity fields were obtained in the $x-y$ plane at $z/H = 0$ using two-dimensional, two-component PIV measurements. To obtain the velocity field over $0 < x/H < 7.2$ at the desired spatial resolution, a composite data-set was acquired, consisting of four individual PIV measurement fields-of-view (FOV) at various downstream locations. The four FOV were stitched together in post-processing. There was a slight overlap of each of the four FOV. In the overlap region, the same number of vectors from both the upstream and downstream data-sets were removed – no averaging of the data was performed. A high-speed camera (Vision Research, Phantom v1840) with a resolution reduced to 2048×1536 pixel[2] and an 85 mm lens (Zeiss, Planar T* 1,4/85 mm ZF.2) were used to capture images. The magnification factor was 5.95 px/mm. The flow was illuminated by four 100 mJ 532 nm ND:YAG lasers (Innolas, Spitlight DPSS). 8000 PIV snapshots were acquired at 400 Hz. The width of the laser sheet was approximately 3 mm. A smoke machine with a glycol smoke fluid was used to seed the flow. In–house cross-correlation software, originally developed by Fouras et al. (2008), was used to correlate interrogation windows of final size 16×16 pixel[2,] with an overlap of 50%, to obtain the velocity fields. This corresponded to a composite velocity vector field of approximately 1000×191 vectors[2] with a spatial resolution of 0.015×0.015 H^2 (2.69×2.69 mm[2]). The laser, camera, and surface pressure measurements were synchronised using a pulse generator

(Quantum Composer, 9530 Series Delay Pulse Generator). With PIV measurements acquired at 400 Hz, frequencies of up to $St_H = 1.8$ (200 Hz) can theoretically be resolved at the operational flow speed. As forcing was imposed at up to $St_H = 1.98$, evidently not all dynamic flow features can be resolved. However, given that the shear-layer and step-mode instabilities are expected to be at $St_\theta \approx 0.012$ ($St_H \approx 0.24$) and $St_H \approx 0.185$ respectively (Hasan, 1992), these key features, along with other large-scale motions of the flow which are of primary interest, can be resolved. To capture details of the flow near separation in greater detail, a second set of PIV data was acquired using a 200 mm lens (Nikon, AF Micro-Nikkor 200 mm F/4D IF-ED), with the laser sheet positioned at $z/H = 1.75$ to provide a magnification factor of 15.22 px/mm. This resulted in a spatial resolution of 0.006×0.006 H^2 (1.05×1.05 mm[2]). Other settings were the same as for the general composite FOV.

3. The effect of Reynolds number on the natural response

Among the key features of the BFS flow that have been extensively studied, the mean reattachment length has received the most attention. Here, the mean reattachment length is determined by finding the point of zero mean streamwise velocity at progressively lower vector locations and extrapolating those points to the step floor. It is important to note that this point only exists in the mean sense – multiple locations of zero streamwise velocity may exist instantaneously, and can fluctuate in position on the order of ± 1 H. As discussed in the introduction, the mean reattachment length can vary with an alteration of any of several key parameters. Nadge and Govardhan (2014) examined, amongst other things, the variation in reattachment length with Reynolds number and ER over the range $5 \times 10^3 \leqslant Re_H \leqslant 6.7 \times 10^4$. For an ER of 1.1, the value used in the current study, they found that the reattachment length saturates for $Re_H \gtrsim 2 \times 10^4$, although differences in the mean-flow structure remained. More recently, Chovet et al. (2017) found a decreasing trend in reattachment length up to $Re_H = 1.68 \times 10^5$. However, they alluded to the influence of another, unnamed, parameter. Fig. 4 shows the reattachment length for the current study without imposed forcing along with other comparable studies. While the results align well with those of Chovet et al. (2017), and it does appear that overall the reattachment length may be increasing slightly with Reynolds number, no appreciable variation was observed over the factor of three Reynolds number range investigated. It also should be noted that differences in several parameters, some of which are listed in Table 1, may also contribute to differences in the reattachment length between studies.

In addition to information on the global flow structure obtained from PIV, the base and floor pressure profiles provide insight into the forces acting on the geometry. Fig. 5 shows the mean ($C_p = (p - p_{ref})/(0.5\rho U_{ref}^2)$) and standard deviation ($\sigma_{C_p} = \sigma_p/(0.5\rho U_{ref}^2)$) of step floor pressure for the current and comparable studies. Only the
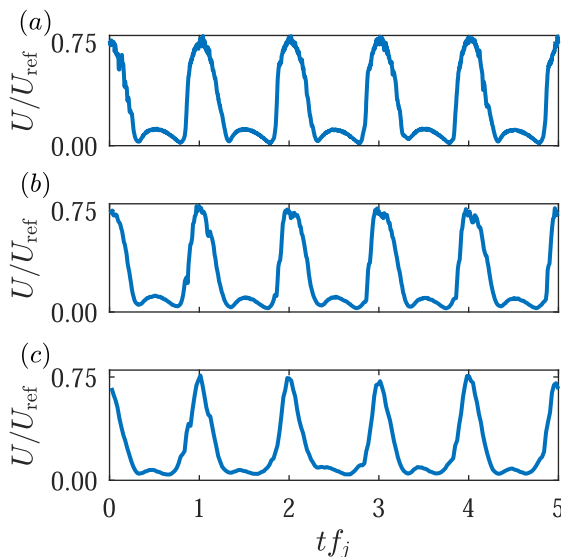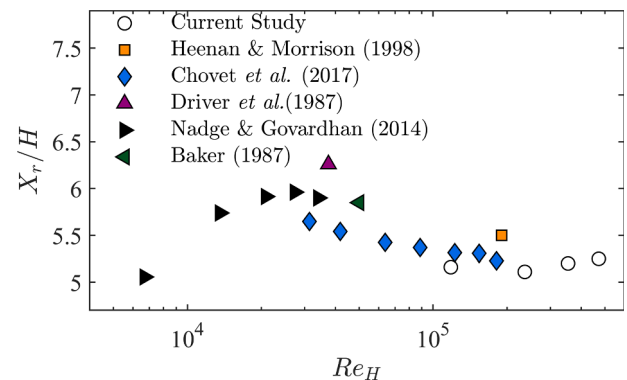
Fig. 3. Velocity signals obtained from the hot-wire measurements for (*a*) 30 Hz, (*b*) 100 Hz, and (*c*) 220 Hz. The measurements were acquired in the centre-line of the slot, 2 mm from the slot exit.

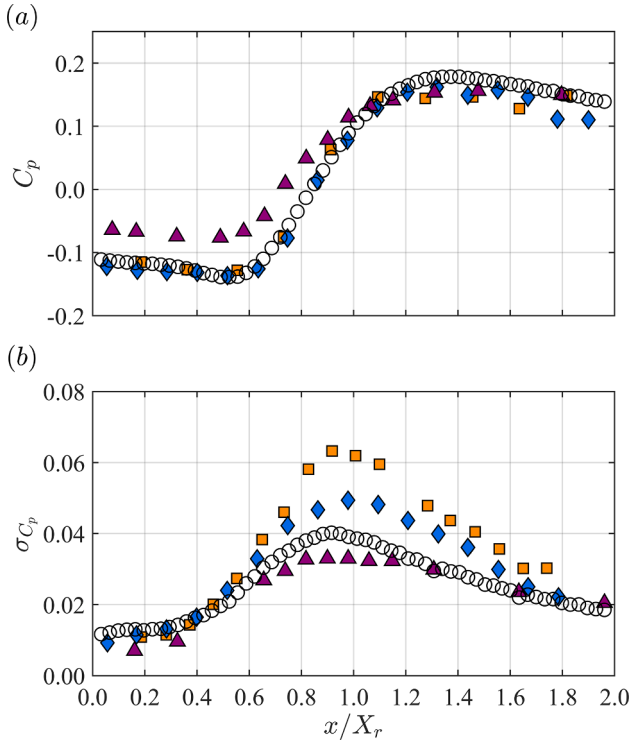**Fig. 4.** Reattachment length against Re_H for the current and comparable studies.

Fig. 5. Mean (*a*) and standard deviation (*b*) of pressure on the step floor. Results shown are for the current study (at $Re_H = 4.72 \times 10^5$) (○); Heenan and Morrison (1998) (■); Chovet et al. (2017) at $Re_H = 1.83 \times 10^5$ (◆); Driver et al. (1987) (▲).

results for the highest Reynolds number are shown as no appreciable variation in either the mean or standard deviation of pressure were observed over the Reynolds number range tested. The mean pressure distribution closely matches that of Chovet et al. (2017) and Heenan and Morrison (1998), who conducted testing at $Re_H \approx 2 \times 10^5$. More variation between studies can be observed in the magnitude of the pressure fluctuations and, to a lesser extent, the position of the maximum standard deviation in relation to the reattachment position (Fig. 5 (*b*)). The location of maximum σ_{C_p} occurs just upstream of reattachment, which has been previously reported for the BFS as well as other reattaching flows [see] (Lee and Sung, 2001). Chovet et al. (2017) noted that this position is sensitive to both the boundary-layer height and the *ER* and that for higher *ER* the peak in σ_{C_p} occurs further upstream from reattachment. The variation in the magnitude of the fluctuations may be primarily attributed to the inverse relationship between boundary-layer thickness and turbulent fluctuations near reattachment (Adams and Johnston, 1988).

3.1. The effect of forcing

Fig. 7 shows the effect of forcing on the mean base pressure — which can be viewed as a proxy for drag — over the non-dimensional frequency range $0.036 \leqslant St_H \leqslant 1.98$ and amplitude range $0.25 \leqslant U_j/U_{\mathrm{ref}} \leqslant 0.75$ compared to the natural response ($\overline{C_{p,o}}$). Fig. 7 reveals large base pressure and reattachment length reductions when forcing at frequencies around the step-mode ($St_H \approx 0.185$) and shear-layer instabilities ($St_\theta \approx 0.012$ ($St_H \approx 0.24$)) identified by Hasan (1992). Comparisons may be drawn here to the base pressure reduction, and corresponding drag increase, of three-dimensional bluff bodies with imposed forcing. For a square-back bluff body with forcing near the wake-mode, at higher frequencies associated with certain shear-layer modes, Barros et al. (2016a, b) observed a shortening of the recirculation zone and significant base pressure reduction. For forcing frequencies larger than

approximately five times the step-mode instability for this study, and ten times the wake-mode of the square-back bluff body, a base pressure increase was achieved. Barros et al. (2016b) attributed the base pressure increase to two mechanisms: a narrowing of the wake, likened to fluidic boat tailing; and a reduction in shear-layer entrainment. Berk et al. (2017) discussed comparable effects of reduced shear-layer entrainment for the BFS. Fig. 6 shows that a comparable wake narrowing, or fluidic boat tailing effect, occurs for high-frequency forcing of the BFS. Barros et al. (2016b) attributed this to the generation of vortex structures by the synthetic jet that induce a cross-stream velocity in a localised area near the slot. The effect here appears comparable to that observed by Barros et al. (2016b), even though the jet is emitted at a 45° angle to the free stream (as opposed to parallel). Further discussion on the mechanism of the base pressure variation for the BFS is continued in Section 3.2.

To investigate the effect of forcing amplitude and select a forcing amplitude for subsequent PIV measurements, the effect of varying peak jet velocity at both low, 20 Hz ($St_H = 0.18$), and high, 220 Hz ($St_H = 1.98$), forcing frequencies was examined. This preliminary testing provided an indication of the sensitivity of forcing amplitude in the low- and high-forcing frequency regimes. There is a similar trend in the base pressure response to forcing amplitude for both forcing frequencies (Fig. 8). An initially strong sensitivity to peak jet velocity precedes a saturated response, up to the highest jet velocities tested. A peak jet velocity of 75% of the freestream flow was selected for PIV measurements as the response has saturated for both low- and high-forcing frequencies. The low forcing frequency selection was subsequently refined to $St_H = 0.27$ and no further analysis conducted at $St_H = 0.18$. All subsequent discussion will focus on results for $U_j/U_{\mathrm{ref}} = 0.75$ for the three forcing frequencies at which PIV measurements were acquired: $St_H = 0.27$, close to the shear-layer instability; $St_H = 1.98$, representative of the shear-layer stabilisation and reduced entrainment regime; and $St_H = 0.9$, a configuration between the previous two.

In addition to the base pressure, Fig. 7 also shows the variation in reattachment length for $U_j/U_{\mathrm{ref}} = 0.75$, at the configurations for which PIV measurements were acquired, compared to the natural response ($X_{r,o}$). Similar trends in base pressure and reattachment length variation
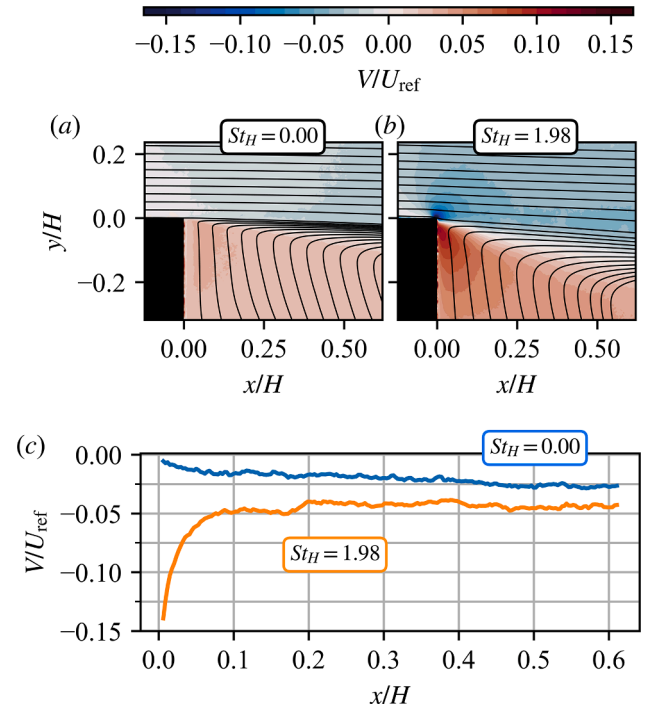

Fig. 6. Mean velocity streamlines and colour contours of vertical velocity for the natural response (*a*) and with imposed forcing at $St_H = 1.98$ (*b*). (*c*) Vertical velocity at $y/H = 0$.

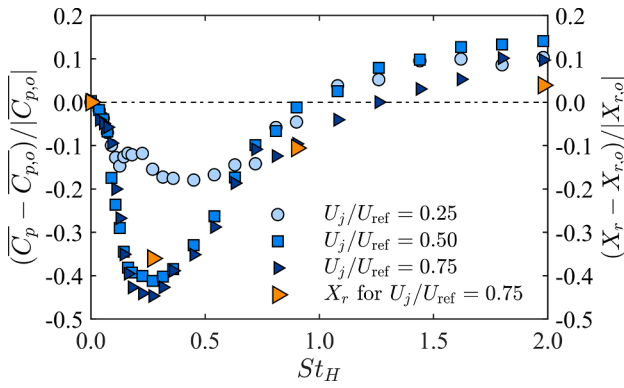**Fig. 7.** Variation in mean step base pressure (blue markers) and reattachment length (orange markers) from the natural response at $Re_H = 2.36 \times 10^5$. The black dashed line indicates the natural response.
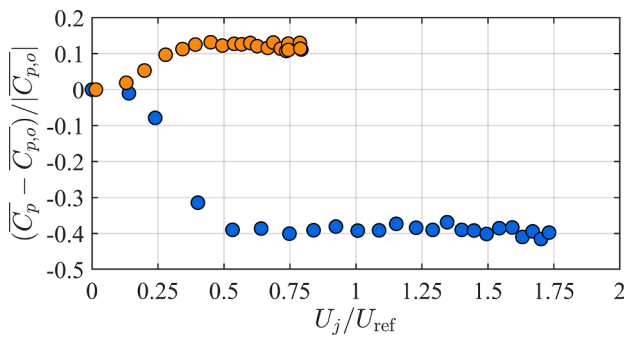

Fig. 8. Variation in mean base pressure against peak jet velocity for forcing at 20 Hz ($St_H = 0.18$) (●) and 220 Hz ($St_H = 1.98$) (●).

with forcing frequency are evident. A reduction in mean base pressure ($\overline{C_p}$) of up to 45% and reattachment length of 36% occurred when forcing close to the shear-layer instability frequency (Hasan, 1992) at $St_\theta = 0.0137$ ($St_H = 0.27$). This minimum in the reattachment length with imposed forcing close to the shear-layer instability has been reported in many previous studies [e.g.] (Chun and Sung, 1996; Ma et al., 2015; Chovet et al., 2019). Forcing in the proximity of the shear-layer instability leads to the early development of a well organised vortex street, with the presence of strong periodic vortex structures, resulting in increased momentum transfer into the recirculation zone and a reduction of the reattachment length (Benard et al., 2016; Berk et al., 2017). At the highest forcing frequency implemented in this investigation, $St_\theta = 0.101$ ($St_H = 1.98$), an increase in mean base pressure of up to 9.7% and reattachment length of 3.9% was observed.

In regard to the base pressure response, Dahan et al. (2012) conducted a numerical study on the effect of both open- and closed-loop flow control on the base pressure of a BFS. Their work consisted of three-dimensional simulations at $Re_\theta = 1500$, with a turbulent incoming boundary layer and actuation from the top corner of the step. A similar trend in reattachment length to that observed in the current study was reported. However, there was more variation in the base pressure response between the two studies. Dahan et al. (2012) found an increase in base pressure when forcing at $St_H < 0.1$, which was not observed in the current study. They found the minimum base pressure close to the forcing frequency that resulted in the minimum reattachment length, a result that closely matched the current study. However, they observed an up to approximately 150% reduction in base pressure as opposed to only the 45% reduction observed here. For forcing at $St_H > 3$, they observed a base pressure increase, whereas here an increase was observed for $St_H > 1$. Although there are several differences between the studies, including variations in AR, wall boundary

conditions, jet velocity uniformity, and boundary layer height, perhaps of most interest is the higher Reynolds number in this study, of roughly an order of magnitude ($Re_\theta = 11,800$ compared to $Re_\theta = 1500$). It is often found that the control of flow becomes more difficult as Reynolds number (and the associated turbulent fluctuations) increases. These results suggest that may be the case for the BFS. Regardless, aside from the variation in magnitude, the trends of base pressure reduction when forcing near the shear-layer instability, and base pressure increase when forcing at high frequencies, were common between the studies.

The distinct change in the global flow structure with imposed forcing can be seen in Fig. 9, which shows streamlines of the mean flow and colour contours of the out-of-plane component of vorticity (ω_z). For all three forcing conditions, immediately downstream of separation there is a broader region (in the wall-normal direction) of more intense vorticity, which can be attributed to the generation of stronger vortex structures due to the imposed forcing at the step top corner. For forcing at $St_H = 0.27$, the shear layer bends downwards over a shorter streamwise distance, impacting the step floor at a steeper angle and resulting in a significantly reduced reattachment length. The size of the counter-rotating corner vortex (centred around $x/H = 0.3, y/H = -0.8$ for the natural response) is also significantly reduced with imposed forcing at $St_H = 0.27$. Interestingly, for the highest forcing frequency, even though there is minimal variation in the reattachment length, the corner vortex remains smaller than for the natural response and the main recirculation bubble is stretched in the streamwise direction, extending upstream to the base over a greater portion of the step height.

In addition to the changes in mean flow structure, there is significant variation in the base and floor pressure profiles with imposed control. The rise in floor pressure, seen across reattachment, shifted upstream for forcing at $St_H = 0.27$ (Fig. 10 (a)), concomitant with the change in reattachment length. For all forcing frequencies, there was no appreciable change in the maximum floor pressure. However, in the recirculation region, there are changes to the minimum floor pressure. For $St_H = 0.27$, a lower minimum floor pressure occurs closer to the base. For high-frequency forcing, comparing the natural response with actuation at $St_H = 1.98$, it can be seen that only upstream of $x/H \approx 4$ is there noticeable variation between the two profiles, with a small increase in
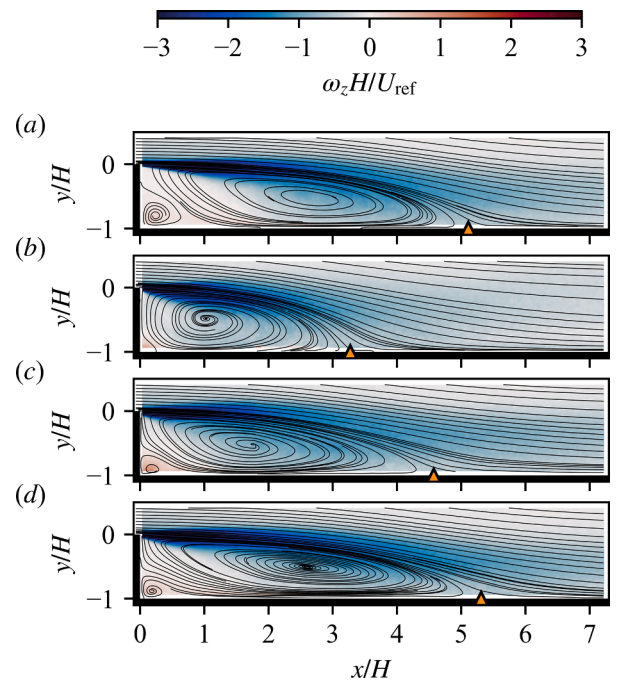

Fig. 9. Mean velocity streamlines and colour contours of out-of-plane vorticity (ω_z) for the natural response (a), and forcing at $St_H = 0.27$ (b), $St_H = 0.9$ (c), and $St_H = 1.98$ (d). The ▲ markers indicate the mean reattachment length.
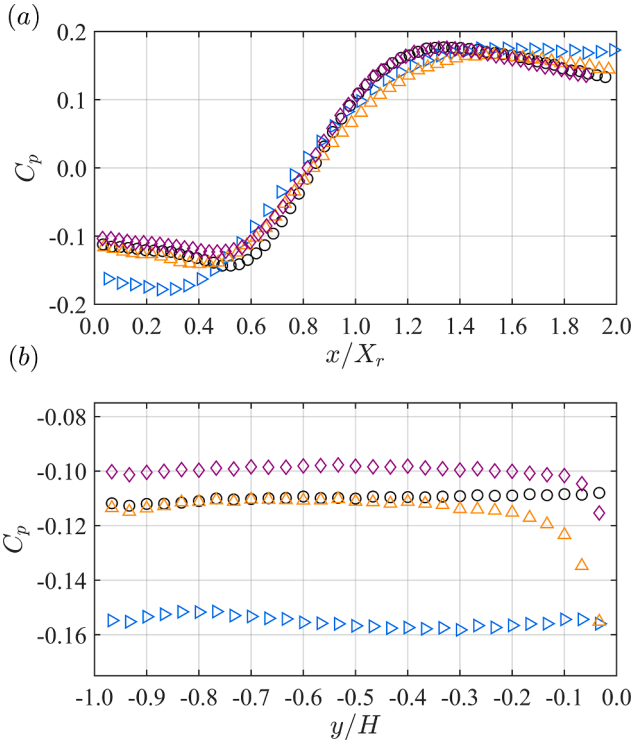
Fig. 10. Mean floor (*a*) and base (*b*) pressure for the natural response (○) and forcing at $St_H = 0.27$ (▷), $St_H = 0.9$ (△), and $St_H = 1.98$ (◇).

Fig. 11. Standard deviation of floor (*a*) and base (*b*) pressure for the natural response (○) and forcing at $St_H = 0.27$ (▷), $St_H = 0.9$ (△), and $St_H = 1.98$ (◇).

the floor pressure occurring throughout the majority of the recirculation region.

The differences observed in the floor pressure profiles in the recirculation zone are highlighted in Fig. 10 (*b*), which shows the base pressure profiles. For $St_H = 0.27$, like for the natural response, there is only minimal variation in the pressure distribution along the base. For high-frequency forcing however, significant variation in mean pressure was observed close to the top of the step, near where the pulsed jet is emitted. This drop-off in pressure near the top corner can be attributed to the formation of strong vortex structures a very short distance downstream of separation with imposed forcing at high frequencies.

As might be expected, forcing close to the shear-layer instability ($St_H = 0.27$) results in significantly increased wall pressure fluctuations in the reattachment region, with peak standard deviation of floor pressure approximately twice that of the natural response (Fig. 11 (*a*)). Forcing at $St_H = 0.9$ resulted in a relatively flat standard deviation of wall pressure through the recirculation region. With forcing at $St_H = 1.98$, there is no appreciable difference in the standard deviation of wall pressure in comparison to the natural response for $x/X_r > 0.7$. However, moving upstream towards the step base, the standard deviation of pressure with imposed forcing increases above the natural response. For forcing at $St_H = 0.27$ and $St_H = 1.98$, where there is a distinct peak in the fluctuations, there is no appreciable change in the streamwise location of the peak pressure fluctuations in relation to the reattachment position. On the step base itself, there is a flat response in standard deviation of pressure for the natural case and forcing at $St_H = 0.27$. For forcing at $St_H = 0.9$, there is a peak at $y/H \approx -0.15$. For forcing at $St_H = 1.98$, there is a large peak at the top step corner. Like for the mean pressure profiles, these peaks may be attributed to the proximity and size of the vortex structures shed downstream of separation due to the imposed forcing.

The mean velocity and surface pressure measurements revealed that there was significant variation in the global flow structure with imposed forcing. To determine the variation in turbulent fluctuations throughout the flow, three components of Reynolds stress ($\overline{u'^2}/U_{ref}^2$, $\overline{v'^2}/U_{ref}^2$, and
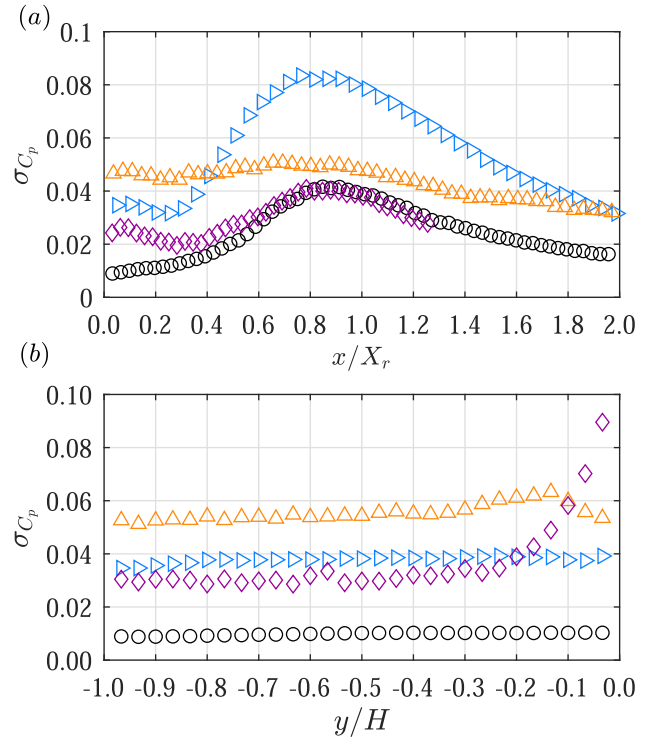
$-\overline{u'v'}/U_{ref}^2$) were examined. For the natural case, all three components of Reynolds stress begin to increase immediately downstream of separation, and continue to do so as the shear layer develops (Driver and Seegmiller, 1985) (Figs. 12–14). The three components all peak in the shear layer upstream of reattachment at $x/H \approx 4$, and are inhibited thereafter as the shear layer approaches the step floor (Ma and Schröder, 2017). Similar spatial distributions are observed with imposed forcing. However, for the wall-normal component ($\overline{v'^2}/U_{ref}^2$) in particular
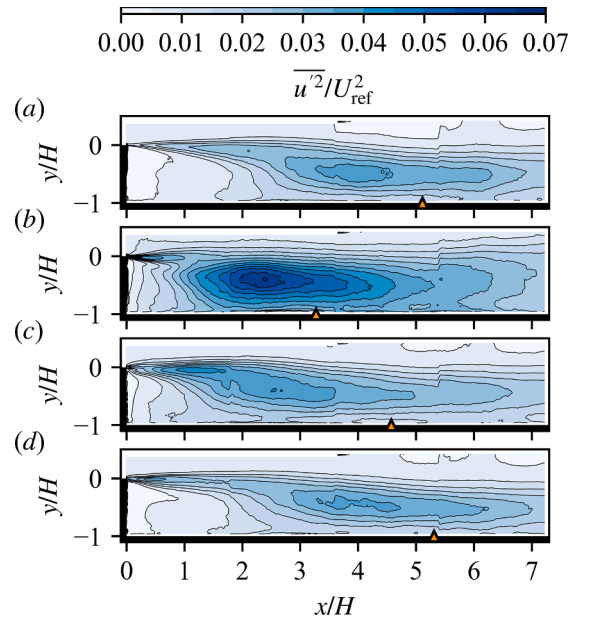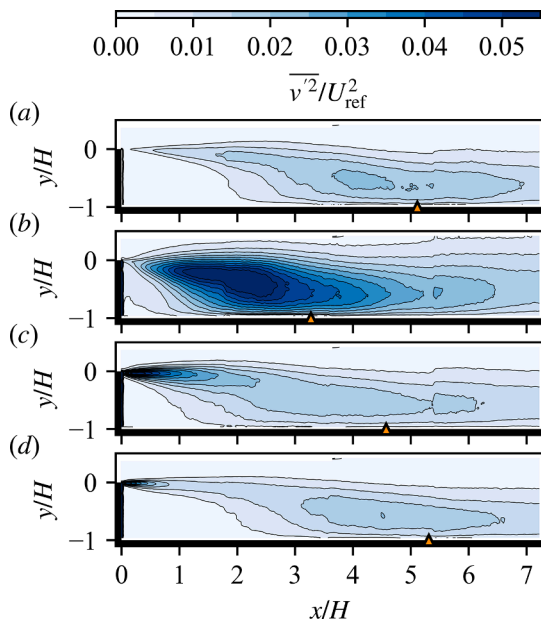

Fig. 12. Normalised streamwise component of Reynolds stress ($\overline{u'^2}/U_{ref}^2$) for the natural response (*a*) and forcing at $St_H = 0.27$ (*b*), $St_H = 0.9$ (*c*), and $St_H = 1.98$ (*d*). The ▲ markers indicate the mean reattachment length.

Fig. 13. Normalised wall-normal component of Reynolds stress ($\overline{v'^2}/U_{ref}^2$). See Fig. 12 for further information.
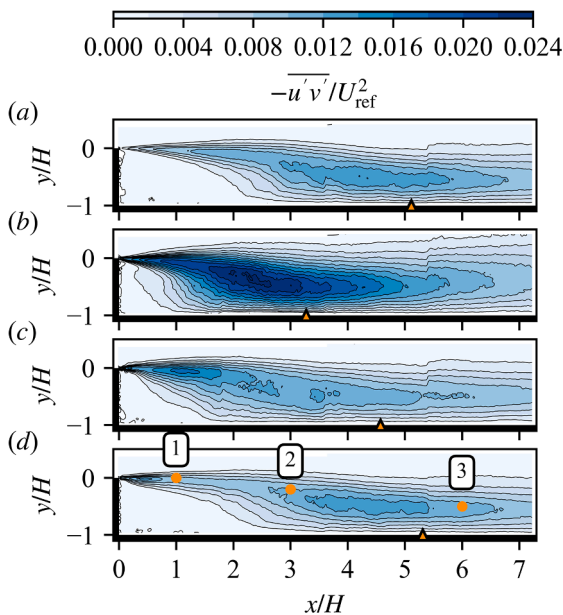

Fig. 14. Normalised shear component of Reynolds stress ($-\overline{u'v'}/U_{ref}^2$). The three labelled positions indicate the locations at which hot-wire measurements were obtained. See Fig. 12 for further information.

(Fig. 13), significantly increased fluctuations are observed just downstream of separation in the shear layer due to the imposed forcing. For forcing at $St_H = 0.27$, the peak shear stress was approximately two times that of the natural response. For $St_H = 1.98$, aside from increased shear stress close to separation, the global distribution and magnitude of shear stress is comparable to the natural response.

To gain a better understanding of the frequency content of the turbulent fluctuations, power spectral density (PSD) estimates obtained from the PIV measurements, along with hot-wire measurements at the three locations depicted in Fig. 14 (c), were examined. The hot-wire measurements were acquired at 3 kHz for 120 s. As the hot-wire measurements were obtained to provide a comparison to PIV, PSD estimates for both measurement techniques were calculated using the same

window length. Therefore, PSD estimates from both measurement techniques will not provide highly accurate resolution of the lowest frequency power content in the BFS flow. Due to the low (compared to the hot-wire measurements) PIV sampling frequency, the PSD estimates obtained from PIV contain more noise than the hot-wire estimates, and frequencies up to only $St_H = 1.8$ can be resolved. However, overall there was good agreement between the PSD estimates obtained from the two measurement techniques. The benefit of using the PIV data for the PSD estimates is that an indication of the distribution of power across the entire spatial domain can be realised. Fig. 15 shows PSD estimates, calculated from the hot-wire data and the streamwise velocity component from the PIV measurements, for the natural response and three forcing conditions at the three locations indicated in Fig. 14 (c). For all forcing conditions at each location, there is significant power associated with the lowest resolvable frequencies. This low-frequency regime is likely associated with the broad-band pulsing, or flapping, of the recirculation zone that several authors have previously identified. Le et al. (1997) conducted direct numerical simulations at $Re_H = 5100$, finding a quasi-periodic behaviour associated with both the reattachment length and pressure fluctuations at $St_H \approx 0.06$. Other authors have found similar peaks in power spectra in the recirculation region around $0.05 < St_H < 0.1$ [e.g.] (Neto et al., 1993; Spazzini et al., 2001). For the natural response, the broad peak at location 1, centred around $St_H \approx 0.28$ ($St_\theta \approx 0.014$), indicates that the shear-layer instability is slightly higher than the $St_\theta \approx 0.012$ identified by Hasan (1992) (who conducted tests at $Re_H = 11\,000$). Further downstream at location 2, this broad peak has reduced in frequency to $St_H \approx 0.2$. This is likely associated with the step-mode instability identified by Hasan (1992), which was observed in the later half of the recirculation region. Downstream of reattachment at location 3, it appears that this broad peak has diminished further and is centred at an even lower frequency.

With imposed forcing at $St_H = 0.27$ (Fig. 15 (b)), at location 1 there is a sharp peak in the spectra at the forcing frequency as well as less distinct peaks at lower and higher harmonics. By location 2, which is near reattachment for forcing at $St_H = 0.27$, there is significant attenuation of all of these peaks aside from the sub-harmonic at $St_H = 0.135$, which may indicate some occurrence of shear-layer vortex merging in this region. For the higher forcing frequencies, the effect of forcing on the power spectra at the three locations at which hot-wire measurements were taken is less prominent.

To view the distribution of spectral power across the spatial domain investigated, the mean power over the frequency ranges indicated by the blue bands in Fig. 15 is plotted in Fig. 16. The PSD estimates determined from the wall-normal component of velocity were used as slightly more power was associated with both the low-frequency flapping motion and shear layer, highlighting the development of these features. Spatial distributions of power of the streamwise velocity component were otherwise very similar. For the natural response (Fig. 16 (a.i)), it can be seen that the low-frequency power band ($0.01 < St_H < 0.08$) is dominant mostly inside the mean recirculation region, from reattachment extending upstream approximately half way to the step base. This region has been identified as the prominent location of the low-frequency flapping behaviour in previous studies. Recently, Ma and Schröder (2017) collated various hypotheses that have been proposed to explain the flapping phenomena and conducted their own experiments to provide further insight. They found that the shear layer begins to flap up and down, starting from the middle of the recirculation region where the spatial development of the shear layer reaches a scale equivalent to the step height. They also found the flapping motion alters the recirculation region and changes the reattachment location. These motions were attributed to an absolute instability, with a highest growth rate where the maximum reverse flow occurs in the recirculation region, as first identified by Wee et al. (2004). With imposed forcing, the spatial distribution of the low-frequency power remains relatively consistent in relation to the base and mean reattachment location (Fig. 16 (b.i,c.i,d.i)).

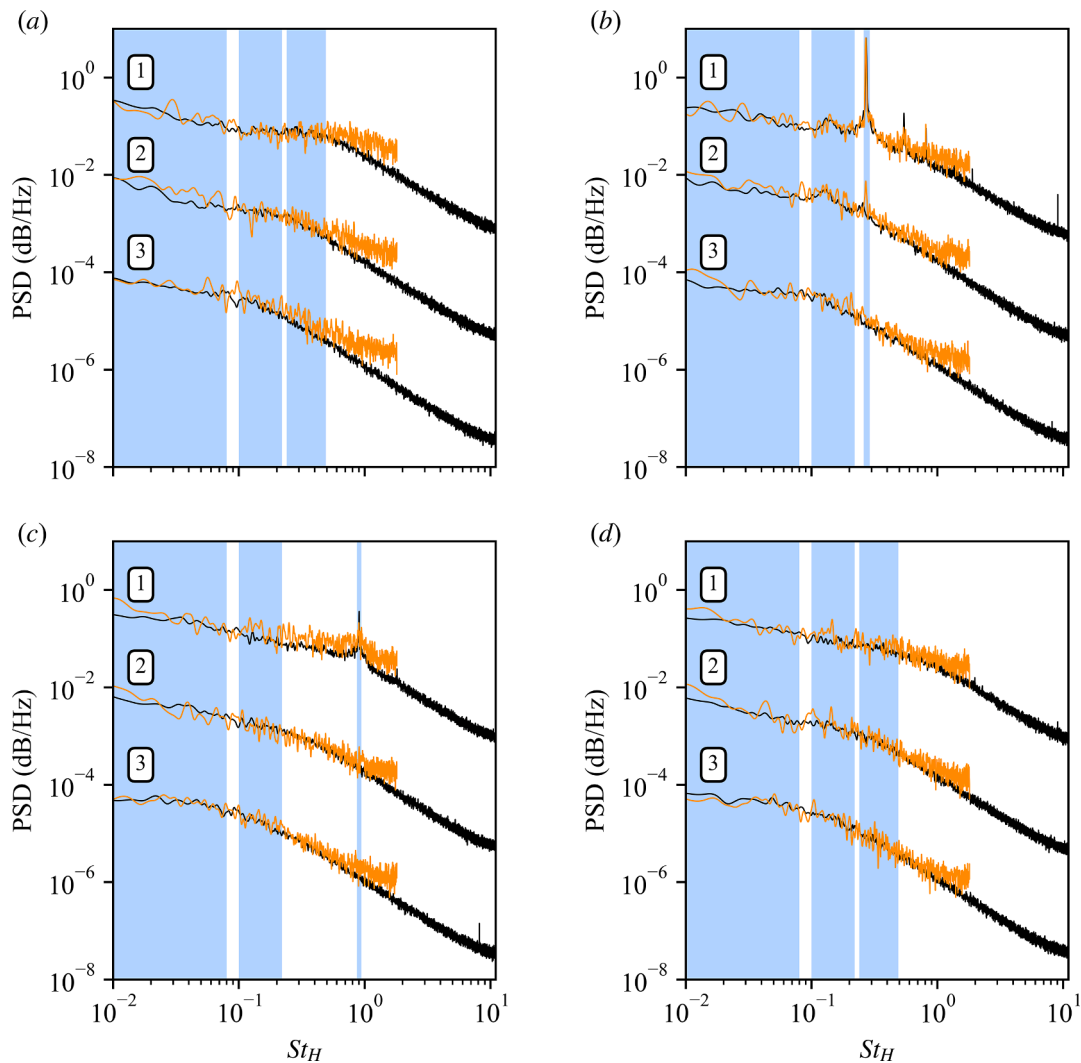The medium-frequency band ($0.1 < St_H < 0.22$), associated with the

Fig. 15. PSD estimates calculated from the streamwise component of PIV measurements (orange) and hot-wire measurements (black) for the natural response (*a*) and forcing at $St_H = 0.27$ (*b*), $St_H = 0.9$ (*c*), and $St_H = 1.98$ (*d*). Each PSD estimate is separated by two decades. The blue bands indicate regions over which the average power was plotted across the spatial domain in Fig. 16. The numbered markers correspond to the positions in Fig. 14 (*c*). (For interpretation of the references to colour in this figure legend, the reader is referred to the web version of this article.)

frequency of roll up of vortices in the shear layer and their interaction with the step floor (Hasan, 1992), again shows a similar spatial distribution for the natural response and all forcing conditions. Fig. 16 (*a.ii,b.ii,c.ii,d.ii*) show that this medium-frequency band builds in power in the shear layer in the latter half of the recirculation region, and persists downstream of reattachment. The peak power across the medium-frequency band for the natural response and all forcing conditions is close to the step floor around the mean reattachment location.

For the natural response, the high-frequency power band ($0.24 < St_H < 0.49$) (Fig. 16 (*a.iii*)) shows the spatial distribution of power around the shear-layer instability frequency. The spectral power in this frequency band grows almost immediately downstream of separation, reaching peak values at $x/H \approx 2$, although it remains close to the maximum power downstream to $x/H \approx 4.5$. For forcing at $St_H = 0.27$ and $St_H = 0.9$, the distribution of power in a narrow frequency band, centred around the imposed forcing frequency, is shown in Fig. 16 (*b.iii, c.iii*). For forcing at $St_H = 0.27$, a well-defined spatial distribution of power centred in the shear layer, extending from near the step downstream to reattachment, is observed. For higher frequency forcing at $St_H = 0.9$, the spectral power at the forcing frequency is stronger immediately downstream of separation, although this only persists downstream to $x/H \approx 1$. Unfortunately, the highest forcing frequency

cannot be resolved with the PIV measurements. Comparing the distribution of power at the forcing frequency for $St_H = 0.27$ and $St_H = 0.9$, and examining instantaneous PIV snapshots, it is evident that higher forcing frequencies result in both the earlier development and diffusion of vortex structures in the shear layer. Therefore, it is expected that, for forcing at $St_H = 1.98$, the region of peak spectral power would occur closer again to the step edge, and that it would persist for only a short distance downstream ($x/H < 1$).

3.2. Discussion on link between forcing frequency and base pressure

In the previous section, the effects of low- and high-frequency forcing on the mean flow structure, turbulent fluctuations, and frequency content of the turbulent fluctuations were examined. As previous studies have shown [e.g.] (Chun and Sung, 1996; Yoshioka et al., 2001), the reattachment length can be shortened by imposing forcing around the shear-layer instability which enhances momentum transfer into the recirculation zone. Conversely, it can be lengthened slightly by forcing at high frequencies to stabilise the instability and prevent flow entrainment into the recirculation zone (Berk et al., 2017). A discussion on the effects of forcing in these two regimes on the global flow structure and base pressure follows.
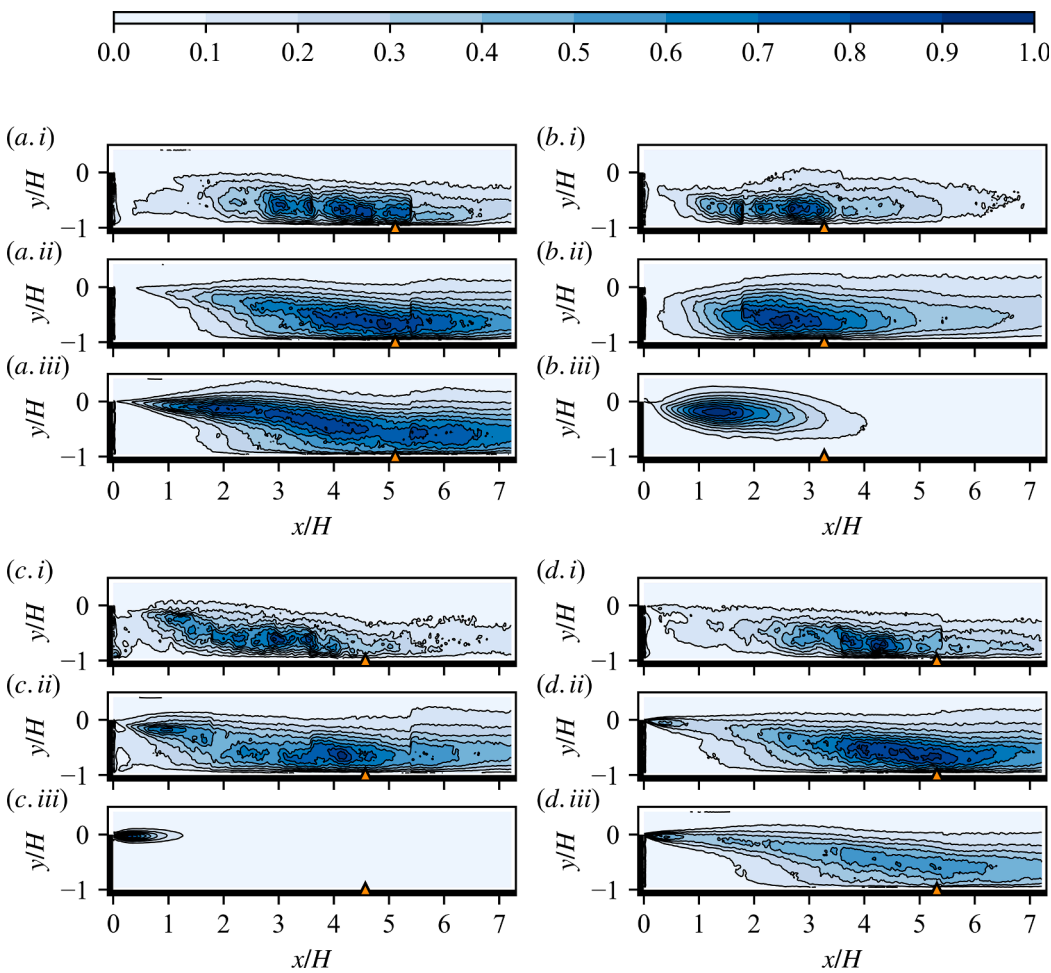
Fig. 16. Spatial distribution of mean power of the wall-normal velocity component for the natural response (*a*), and imposed forcing at $St_H = 0.27$ (*b*), $St_H = 0.9$ (*c*), and $St_H = 1.98$ (*d*) over the frequency ranges: $0.01 < St_H < 0.08$ (*i*); $0.1 < St_H < 0.22$ (*ii*); and $0.24 < St_H < 0.49$ (*iii*) for (*a*) and (*d*), and a narrow band around the forcing frequency for (*b*) and (*c*). Power has been normalised by the peak power across the spatial domain. See Fig. 15 for a visual representation of these frequency ranges. The ▲ markers indicate the mean reattachment length.

The dominant and highly periodic behaviour of the fluctuations with imposed forcing close to the shear-layer instability ($St_H = 0.27$) makes this configuration an ideal candidate for phase-averaging. With a similar set-up, albeit at lower Reynolds numbers, Benard et al. (2016) used plasma actuators to impose forcing near the shear-layer instability frequency. They examined the phase-averaged velocity field (using the λ_2-criterion), finding the shedding of large-scale vortex structures that persisted downstream of reattachment. They demonstrated that those structures have a distinct influence on the reattachment length as they pass through the reattachment zone, resulting in a relatively periodic oscillation of the phase-averaged reattachment location.

A similar phase-averaging analysis technique was employed here. Using the pressure tap on the step base 6 mm (0.03 y/H) below the actuation slot, 8000 PIV snapshots were divided into 24 phases. Fig. 17 shows the phase-averaged velocity vectors and contours of the Γ_2 criterion (Graftieaux et al., 2001) for forcing at $St_H = 0.27$, with four phases separated by a quarter cycle. The formation and convection of large-scale, clockwise-rotating structures that persist past reattachment is evident. Examining surface pressure measurements, local minima in the base and step-floor pressure profiles that convect downstream with the passing of these large-scale structures was visible. Lastly, a small counter-clockwise-rotating corner vortex that is relatively stable in size and position across all phases can be seen.

From Fig. 17, some oscillatory motion of the reattachment location can be seen to occur. To examine this further, the phase-averaged reattachment location and step base pressure is plotted in Fig. 18. The phase-averaged reattachment location resembles a triangular profile, varying between $x/H \approx \pm 0.2$. Benard et al. (2016) found the same phase-averaged profile of reattachment length variation, demonstrating
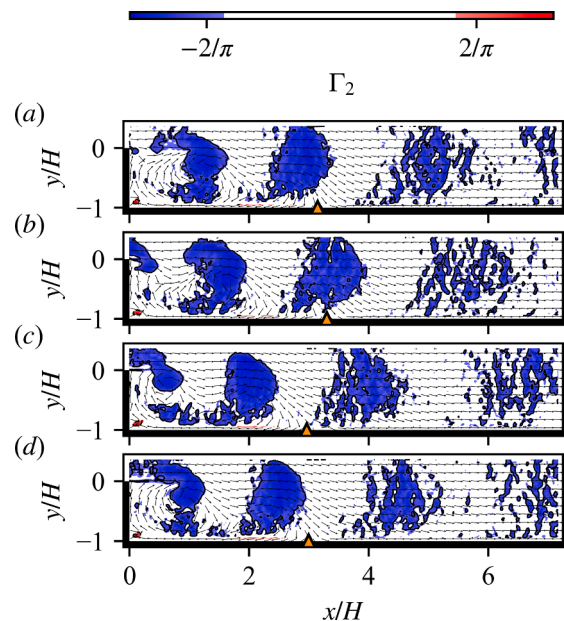

Fig. 17. Phase-averaged velocity vectors and colour contours of the Γ_2 with imposed forcing at $St_H = 0.27$. Each plot is separated by a quarter cycle. Blue contours show clockwise rotation, red contours show counter-clockwise rotation. The ▲ markers indicate the mean reattachment length. (For interpretation of the references to colour in this figure legend, the reader is referred to the web version of this article.)
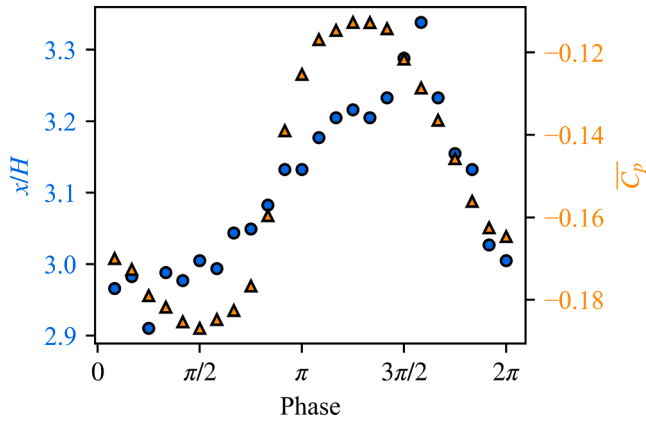
Fig. 18. Phase-averaged reattachment length (●) and mean base pressure (▲) with imposed forcing at $St_H = 0.27$.

how the maximum reattachment location occurred with a vortex structure passing over reattachment, and a minimum when reattachment occurred between two vortex structures. The phase-averaged base pressure resembles more of a sinusoidal profile and appears to be primarily influenced by the generation and initial development of the strong vortex structures relatively close to the base, as opposed to the motion of the fully developed structures.

Figs. 19 and 20 show mean streamwise and wall-normal velocity profiles at various downstream locations. The profiles show, in general, higher velocity in the recirculation region for $St_H = 0.27$. This affects the overall reattachment length by the strong vortex structures combining, which enhances momentum transfer into the recirculation region. This is associated with shear layer development, such that it curves more quickly to the step floor. This causes a more intense flow recirculation and low mean base pressure, with higher fluctuations than for the natural response.

For high-frequency forcing ($St_H = 1.98$), the differences to the natural response are more subtle. From the plots of Reynolds stress components, mean step floor pressure profiles, and the velocity profiles
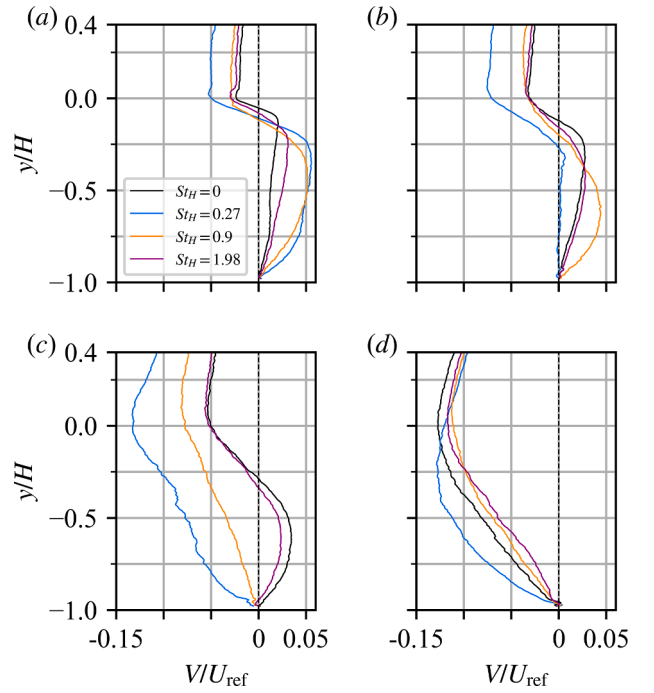

Fig. 19. Streamwise velocity at: $x/H = 0.5$ (a); $x/H = 1$ (b); $x/H = 2$ (c); and $x/H = 4$ (d).

Fig. 20. Wall-normal velocity at: $x/H = 0.5$ (a); $x/H = 1$ (b); $x/H = 2$ (c); and $x/H = 4$ (d).

shown in Figs. 19 and 20, it is evident that the later half of the recirculation zone appears very similar to the natural response when the high-frequency forcing is imposed. In particular, the streamwise velocity profiles at $x/H = 2, 4$ (Fig. 19(c, d)) show only minimal variation. From Fig. 20(c, d), slightly more variation in wall-normal velocity can be seen, with a reduction in magnitude in the recirculation region at $x/H = 2, 4$ when forcing is imposed. There is also a slight reduction in the wall-normal component of Reynolds stress at these locations with imposed high-frequency forcing. Furthermore, a slight change occurs in the hot-wire power spectra measured at locations 1 and 2 (shown in Fig. 14(c)), which has been plotted in Fig. 21. At location 1, a reduction in spectral power over the broad region associated with the natural shear-layer instability and a slight increase at higher frequencies centred around the forcing frequency is evident when there is imposed high-frequency forcing. Further downstream at location 2, no increase in spectral power around the forcing frequency was observed. However, there remains a slight reduction in spectral power over the broad peak now centred close to the step-mode instability. From the spatial distribution of spectral power across the low-frequency band (re-plotted in Fig. 22 with raw power values), there also appears to be a slight reduction in the power associated with the low-frequency flapping motion.

As shown by past studies, the high-frequency forcing disrupts the initial development of the shear layer, which reduces momentum transfer into the recirculation region. In this study it was shown that this ultimately results in less intense velocity fluctuations near reattachment and slightly reduced spectral power associated with the flapping motion. This effect also translates to noticeable variation in the instantaneous reattachment length. Fig. 23 shows the instantaneous reattachment length determined by calculating the streamwise positions of zero streamwise velocity, averaged in space (in the wall-normal direction over $-1 < y/H < 0.95$) and time (over 10 PIV snapshots, $T^* = tU_{ref}/H \approx 2.5$). While the reattachment length can only really be defined in the mean sense, Fig. 23 offers insight into and some measure of quantification of the fluctuations that occur in the reattachment region. Note that, as discussed, the four individual PIV measurements compiled to show the whole spatial domain of interest are not correlated in time. As such, the sub-plots of reattachment length shown in Fig. 23 only
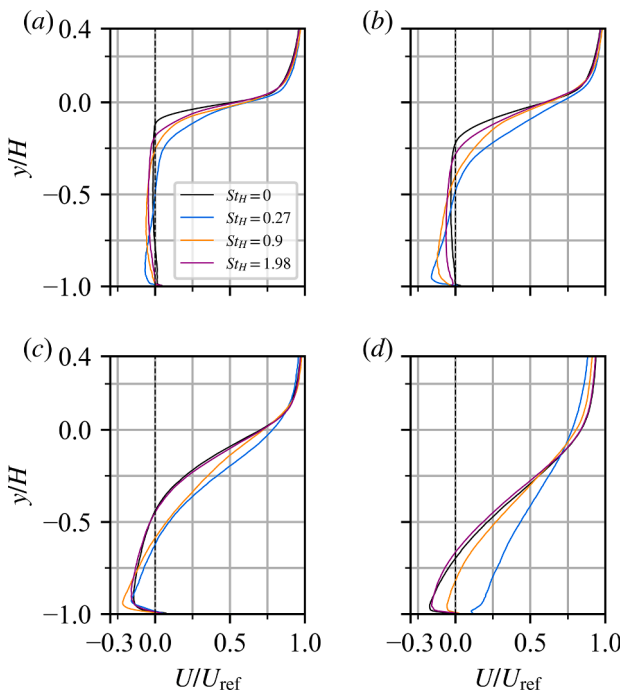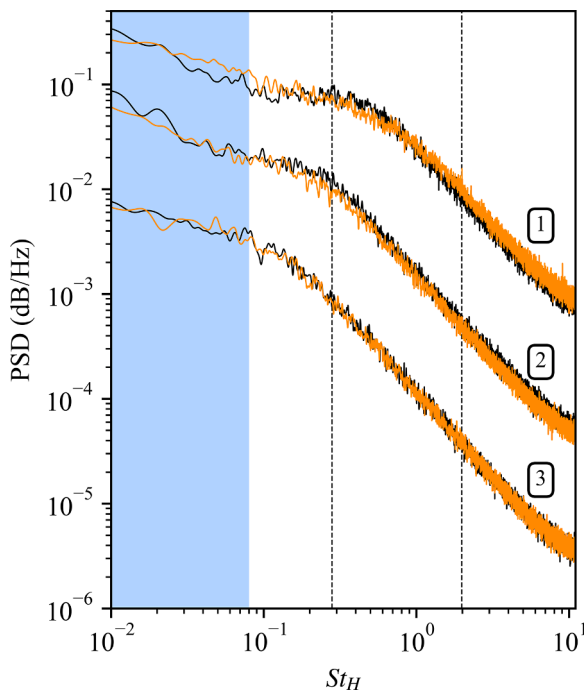
Fig. 21. PSD estimates calculated from hot-wire measurements for the natural response (black) and with imposed forcing at $St_H = 1.98$ (orange). Each PSD estimate is separated by two decades. The blue band indicates the region over which the average power was plotted across the spatial domain in Fig. 22. The numbered markers correspond to the positions in Fig. 14 (d). The black dashed lines indicate the approximate shear-layer instability frequency ($St_H \approx 0.28$, $St_\theta \approx 0.014$) and the forcing frequency ($St_H = 1.98$). (For interpretation of the references to colour in this figure legend, the reader is referred to the web version of this article.)
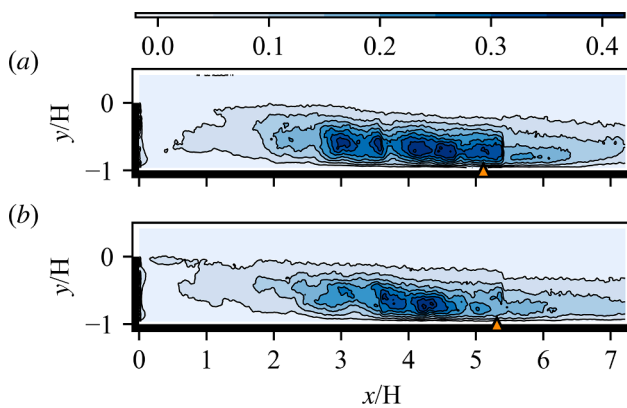

Fig. 22. Spatial distribution of mean power of the wall-normal velocity component over the frequency range $0.01 < St_H < 0.08$ for the natural response (a) and with imposed forcing at $St_H = 1.98$ (b). See Fig. 21 for a visual representation of this frequency range. The ▲ markers indicate the mean reattachment length.

provide an indication of the magnitude and general trend of variation in reattachment length. Comparing the instantaneous reattachment location for the natural response (Fig. 23 (a)) and high-frequency forcing (Fig. 23 (d)), it is evident that less streamwise fluctuation of the reattachment length occurs with imposed forcing. The standard deviation of the calculated instantaneous reattachment length was: $0.39H$ for the natural response; $0.45H$ for forcing at $St_H = 0.27$; $0.67H$ for forcing at $St_H = 0.9$; and $0.30H$ for forcing at $St_H = 1.98$. For the natural response, the time-scale of reattachment location appears to be primarily similar

to the $tU_{ref}/H \approx 17$ scale observed by Le et al. (1997) (which corresponds to $St_H \approx 0.06$). With imposed forcing at $St_H = 1.98$, the time-scale has shortened, with fluctuations primarily occurring in the order of $tU_{ref}/H \approx 8$.

As a result of the reduced intensity of wall-normal fluctuations in the latter half of the reattachment zone and the stabilised reattachment location, there appear to be subsequent effects on the flow entrained far upstream from near reattachment. Combining these findings and examining instantaneous PIV snapshots, for both the natural response and with high-frequency forcing, periods of higher velocity flow moving upstream near the step floor can be observed from close to reattachment. For the natural response, in general, these regions of higher velocity flow are drawn upwards, back into the shear layer due to the relatively high level of turbulent fluctuations. However, with high-frequency forcing, these periods of higher velocity are able to escape being re-ingested into the shear layer and are able to convect far upstream to the base. This increased reverse velocity in the recirculation zone can be seen in Fig. 19 (a, b) at $x/H = 0.5, 1$. These periods of higher reverse flow, moving upstream to thebase, increase both the mean (Fig. 10 (b)) and standard deviation (Fig. 11 (b)) of base pressure, and reduce the size of the counter-rotating corner vortex in comparison to the natural response.

4. Conclusions

The flow over a BFS with imposed periodic actuation has been investigated at higher Reynolds numbers than previous studies. For the natural response, it was found that no significant variation in the global flow structure or reattachment length occurs over the range $1.18 \times 10^5 < Re_H < 4.72 \times 10^5$, which is a levelling out from the decreasing trend previously observed at lower Reynolds numbers. Similar variation in reattachment length with imposed forcing to that previously reported was found, with a maximum reduction of 36% when forcing near the shear-layer instability, and an increase of 3.9% at high-forcing frequencies ($St_H = 1.98$). There has been minimal work investigating the base pressure for the BFS flow. A comparison was made to the numerical study of Dahan et al. (2012). A similar trend in base pressure variation found, with a maximum reduction of 45% when forcing near the shear-layer instability, and an increase of up to 9.7% when forcing at $St_H = 1.98$. While the trend in base pressure variation was comparable, the magnitude of the reduction when forcing near the shear-layer instability was significantly less, suggesting that it is likely more difficult to alter the flow dynamics of the BFS as the Reynolds number increases. Spatial distributions of spectral power provided evidence of a region of low-frequency power in the later half of the recirculation zone that corresponded to a frequency range and spatial region previously associated with a flapping motion of the recirculation zone. The spatial distribution of this low-frequency power did not vary with imposed forcing. Examining higher frequencies revealed the spatial distribution of power of the shear-layer and step-mode instabilities (Hasan, 1992), which has not been previously shown. Forcing around the shear-layer instability resulted in significantly increased turbulent fluctuations, with a periodic oscillation of both the instantaneous reattachment location and base pressure. Phase-averaging revealed the formation and subsequent convection of large-scale vortex structures downstream of reattachment. A triangular profile of phase-averaged reattachment length and a sinusoidal profile of base pressure variation were found. The high-frequency forcing at $St_H = 1.98$ appeared to delay development of the shear layer, minimising wall-normal velocity fluctuations near reattachment and reducing instantaneous reattachment-location fluctuation. This enabled increased entrainment of flow upstream to the step base, resulting in both higher mean and standard deviation of base pressure. This mechanism of base pressure increase with forcing has not been previously reported and offers insight into the use of high-frequency actuation for drag or structural loading reduction. It is important to note that, although a reduction in fluctuations in the later half of the recirculation
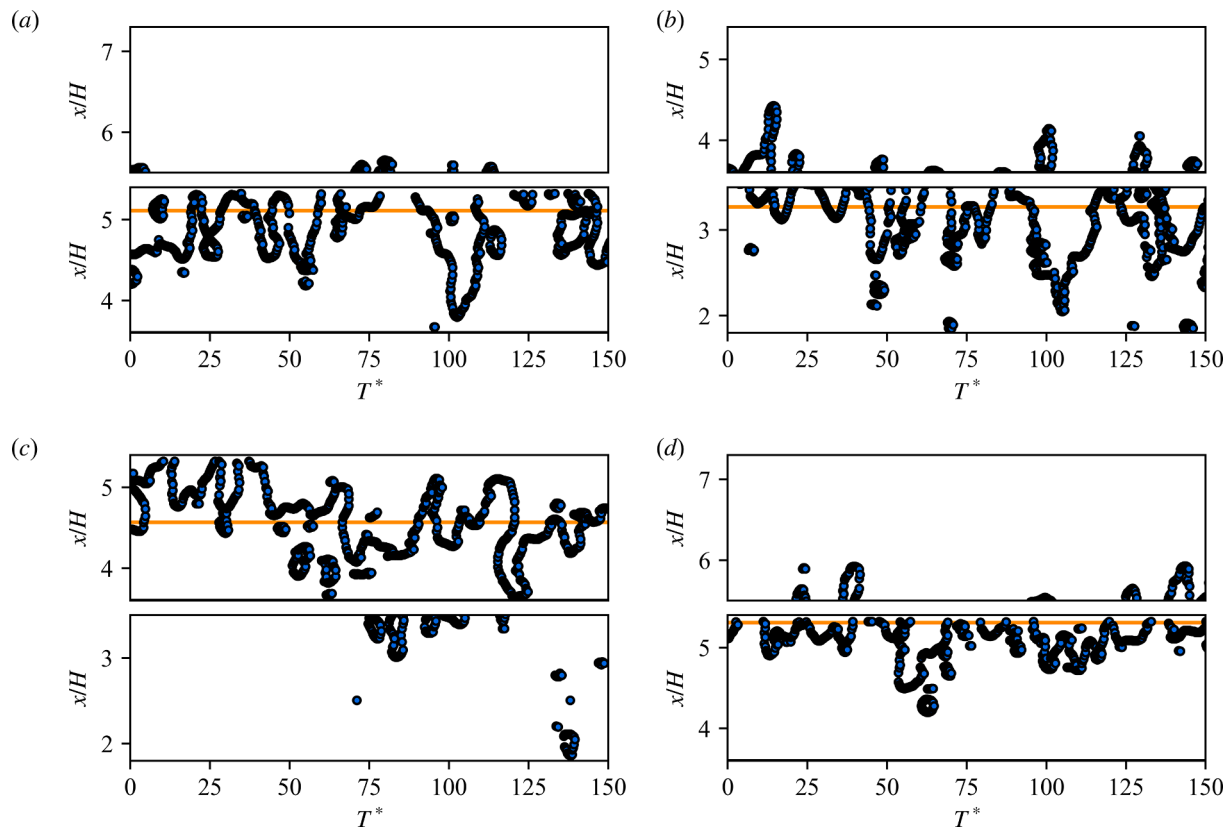
Fig. 23. Instantaneous reattachment length for the natural response (a), and forcing at $St_H = 0.27$ (b), $St_H = 0.9$ (c), and $St_H = 1.98$ (d). Note that the two fields-of-view compiled for each sub-plot are not correlated in time. Each compiled plot merely provides an indication of the extent of reattachment length variation over time. The orange lines indicates the mean reattachment point.

zone and a mean increase in base pressure was achieved with high-frequency forcing, this came at the cost of triple the base-pressure fluctuations, an undesirable characteristic in many practical control applications.

CRediT authorship contribution statement

Thomas McQueen: Conceptualization, Investigation, Software, Data-curation, Formal-analysis, Validation, Writing-original-draft. **David Burton:** Conceptualization, Methodology, Supervision, Resources, Writing-review-editing, Project-administration, Funding-acquisition. **John Sheridan:** Conceptualization, Supervision, Writing-review-editing, Funding-acquisition. **Mark C. Thompson:** Conceptualization, Supervision, Resources, Writing-review-editing, Project-administration, Funding-acquisition.

Declaration of Competing Interest

The authors declare that they have no known competing financial interests or personal relationships that could have appeared to influence the work reported in this paper.

Acknowledgements

References

Adams, E.W., Johnston, J.P., 1988. Effects of the separating shear layer on the reattachment flow structure part 1: pressure and turbulence quantities. Exp. Fluids 6, 400–408. https://doi.org/10.1007/BF00196485. URL:https://doi.org/10.1007/BF00196485.

Baker, S., 1977. Regions of recirculating flow associated with two-dimensional steps. PhD Thesis. Univ. Surrey, Guildford, UK.

Barkley, D., Gomes, M.G.M., Henderson, R.D., 2002. Three-dimensional instability in flow over a backward-facing step. J. Fluid Mech. 473, 167–190. https://doi.org/10.1017/S002211200200232X. URL:https://www.cambridge.org/core/article/threedimensional-instability-in-flow-over-a-backwardfacing-step/EFBE9E8D2D4C261E6702E7918614B360.

Barros, D., Borée, J., Noack, B.R., Spohn, A., 2016a. Resonances in the forced turbulent wake past a 3D blunt body. Phys. Fluids 28, 065104. https://doi.org/10.1063/1.4953176. URL:https://doi.org/10.1063/1.4953176.

Barros, D., Borée, J., Noack, B.R., Spohn, A., Ruiz, T., 2016b. Bluff body drag manipulation using pulsed jets and coanda effect. J. Fluid Mech. 805, 422–459. https://doi.org/10.1017/jfm.2016.508. URL:https://www.cambridge.org/core/article/bluff-body-drag-manipulation-using-pulsed-jets-and-coanda-effect/12609816D2FF77F5372BA9B3E32F69A8.

Benard, N., Sujar-Garrido, P., Bonnet, J.P., Moreau, E., 2016. Control of the coherent structure dynamics downstream of a backward facing step by DBD plasma actuator. Int. J. Heat Fluid Flow 61, 158–173. https://doi.org/10.1016/j.ijheatfluidflow.2016.04.009. URL:http://www.sciencedirect.com/science/article/pii/S0142727X16301448.

Berk, T., Medjnoun, T., Ganapathisubramani, B., 2017. Entrainment effects in periodic forcing of the flow over a backward-facing step. Phys. Rev. Fluids 2, 074605. URL:https://link.aps.org/doi/10.1103/PhysRevFluids.2.074605.

Chandrsuda, C., Bradshaw, P., 1981. Turbulence structure of a reattaching mixing layer. J. Fluid Mech. 110, 171–194. https://doi.org/10.1017/S0022112081000670. URL:https://www.cambridge.org/core/article/turbulence-structure-of-a-reattaching-mixing-layer/AA1D882C0B190558891D8658B27F8210.

Chovet, C., Lippert, M., Foucaut, J.M., Keirsbulck, L., 2017. Dynamical aspects of a backward-facing step flow at large Reynolds numbers. Exp. Fluids 58, 162. https://doi.org/10.1007/s00348-017-2444-5. URL:https://doi.org/10.1007/s00348-017-2444-5.

Chovet, C., Lippert, M., Keirsbulck, L., Foucaut, J.M., 2019. Unsteady behavior of a backward-facing step in forced flow. Flow Turbul. Combust. 102, 145–165. https://doi.org/10.1007/s10494-018-9944-0. URL:https://doi.org/10.1007/s10494-018-9944-0.

Chun, K.B., Sung, H.J., 1996. Control of turbulent separated flow over a backward-facing step by local forcing. Exp. Fluids 21, 417–426. https://doi.org/10.1007/BF00189044. URL:https://doi.org/10.1007/BF00189044.

Dahan, J.A., Morgans, A.S., Lardeau, S., 2012. Feedback control for form-drag reduction on a bluff body with a blunt trailing edge. J. Fluid Mech. 704, 360–387. https://doi.org/10.1017/jfm.2012.246. URL:https://www.cambridge.org/core/article/feedback-control-for-formdrag-reduction-on-a-bluff-body-with-a-blunt-trailing-edge/73733F4D98D5A72EE409DE61FF6CE525.

De Brederode, V., 1975. Three-dimensional effects in nominally two-dimensional flows. PhD Thesis. Imperial College London, London, UK.

Driver, D.M., Seegmiller, H.L., 1985. Features of a reattaching turbulent shear layer in divergent channel flow. AIAA J. 23, 163–171. https://doi.org/10.2514/3.8890. URL:https://arc.aiaa.org/doi/abs/10.2514/3.8890.

Driver, D.M., Seegmiller, H.L., Marvin, J.G., 1987. Time-dependent behavior of a reattaching shear layer. AIAA J. 25, 914–919. https://doi.org/10.2514/3.9722. URL:https://doi.org/10.2514/3.9722.

Eaton, J.K., Johnston, J.P., 1981. A review of research on subsonic turbulent flow reattachment. AIAA J. 19, 1093–1100. https://doi.org/10.2514/3.60048. URL: https://doi.org/10.2514/3.60048.

Fouras, A., Lo Jacono, D., Hourigan, K., 2008. Target-free stereo PIV: a novel technique with inherent error estimation and improved accuracy. Exp. Fluids 44, 317–329. https://doi.org/10.1007/s00348-007-0404-1. URL:https://doi.org/10.1007/s00348-007-0404-1.

Graftieaux, L., Michard, M., Grosjean, N., 2001. Combining PIV, POD and vortex identification algorithms for the study of unsteady turbulent swirling flows. Meas. Sci. Technol. 12, 1422. URL:http://stacks.iop.org/0957-0233/12/i=9/a=307.

Hasan, M.A.Z., 1992. The flow over a backward-facing step under controlled perturbation: laminar separation. J. Fluid Mech. 238, 73–96. https://doi.org/10.1017/S0022112092001642. URL:https://www.cambridge.org/core/article/flow-over-a-backwardfacing-step-under-controlled-perturbation-laminar-separation/20C4F977558D91149B6B6C412098DCF4.

Heenan, A.F., Morrison, J.F., 1998. Passive control of pressure fluctuations generated by separated flow. AIAA J. 36, 1014–1022. https://doi.org/10.2514/2.474. URL: https://doi.org/10.2514/2.474.

Le, H., Moin, P., Kim, J., 1997. Direct numerical simulation of turbulent flow over a backward-facing step. J. Fluid Mech. 330, 349–374. https://doi.org/10.1017/S0022112096003941. URL:https://www.cambridge.org/core/article/direct-numerical-simulation-of-turbulent-flow-over-a-backwardfacing-step/645D21758E8F74568008899C17B12ADD.

Lee, I., Sung, H.J., 2001. Characteristics of wall pressure fluctuations in separated and reattaching flows over a backward-facing step: Part I. Time-mean statistics and cross-spectral analyses. Exp. Fluids 30, 262–272. https://doi.org/10.1007/s003480000172. URL:https://doi.org/10.1007/s003480000172.

Ma, X., Geisler, R., Agocs, J., Schröder, A., 2015. Investigation of coherent structures generated by acoustic tube in turbulent flow separation control. Exp. Fluids 56, 46. https://doi.org/10.1007/s00348-015-1914-x. URL:https://doi.org/10.1007/s00348-015-1914-x.

Ma, X., Schröder, A., 2017. Analysis of flapping motion of reattaching shear layer behind a two-dimensional backward-facing step. Phys. Fluids 29, 115104. https://doi.org/10.1063/1.4996622. URL:https://doi.org/10.1063/1.4996622.

Nadge, P.M., Govardhan, R.N., 2014. High Reynolds number flow over a backward-facing step: structure of the mean separation bubble. Exp. Fluids 55. URL:https://www.scopus.com/inward/record.uri?eid=2-s2.0-84891463875&doi=10.1007%2fs00348-013-1657-5&partnerID=40&md5=dd929e83b4b9a61ab56a272df89a8f85.

Nash, J., 1963. An analysis of two-dimensional turbulent base flow, including the effect of the approaching boundary layer. Report. Aero. Res. Council, Great Britain.

Neto, A.S., Grand, D., Métais, O., Lesieur, M., 1993. A numerical investigation of the coherent vortices in turbulence behind a backward-facing step. J. Fluid Mech. 256, 1–25. https://doi.org/10.1017/S0022112093002691. URL:https://www.cambridge.org/core/article/numerical-investigation-of-the-coherent-vortices-in-turbulence-behind-a-backward-facing-step/872B8F0C8ABDD71FD0582113C20FB858.

Pastoor, M., Henning, L., Noack, B.R., King, R., Tadmor, G., 2008. Feedback shear layer control for bluff body drag reduction. J. Fluid Mech. 608, 161–196. https://doi.org/10.1017/S0022112008002073. URL:https://www.cambridge.org/core/article/feedback-shear-layer-control-for-bluff-body-drag-reduction/F9CEAFA0DF1AE5BC61E8FF425B5D21AA.

Smith, B.L., Glezer, A., 1998. The formation and evolution of synthetic jets. Phys. Fluids 10, 2281–2297. https://doi.org/10.1063/1.869828. URL:https://doi.org/10.1063/1.869828.

Spazzini, P.G., Iuso, G., Onorato, M., Zurlo, N., Di Cicca, G.M., 2001. Unsteady behavior of back-facing step flow. Exp. Fluids 30, 551–561. https://doi.org/10.1007/s003480000234. URL:https://doi.org/10.1007/s003480000234.

Troutt, T.R., Scheelke, B., Norman, T.R., 1984. Organized structures in a reattaching separated flow field. J. Fluid Mech. 143, 413–427. https://doi.org/10.1017/S0022112084001415. URL:https://www.cambridge.org/core/article/organized-structures-in-a-reattaching-separated-flow-field/2267D9D2165490FE4821FE642B3E32B1.

Wee, D., Yi, T., Annaswamy, A., Ghoniem, A.F., 2004. Self-sustained oscillations and vortex shedding in backward-facing step flows: Simulation and linear instability analysis. Phys. Fluids 16, 3361–3373. https://doi.org/10.1063/1.1773091. URL: https://doi.org/10.1063/1.1773091.

Yoshioka, S., Obi, S., Masuda, S., 2001. Organized vortex motion in periodically perturbed turbulent separated flow over a backward-facing step. Int. J. Heat Fluid Flow 22, 301–307. https://doi.org/10.1016/S0142-727X(01)00092-3. URL:http://www.sciencedirect.com/science/article/pii/S0142727X01000923.